PAPER • OPEN ACCESS

WEST full tungsten operation with an ITER grade divertor

To cite this article: J. Bucalossi *et al* 2024 *Nucl. Fusion* **64** 112022

View the article online for updates and enhancements.

WEST full tungsten operation with an ITER grade divertor

J. Bucalossi[1,*], A. Ekedahl[1] (ORCID) and the WEST Team[a]: J. Achard[1], K. Afonin[1], O. Agullo[3], T. Alarcon[1], L. Allegretti[1], F. Almuhisen[1], H. Ancher[1], G. Antar[4], Y. Anquetin[2], S. Antusch[5], V. Anzallo[1], C. Arnas[3], J.F. Artaud[1], M.H. Aumeunier[1], S.G. Baek[6], X.Y. Bai[7], M. Balden[8], C. Balorin[1], T. Barbui[9], A. Barbuti[1], J. Barlerin[1], J. Barra[1], V. Basiuk[1], T. Batal[1], O. Baulaigue[1], A. Bec[1], M. Becoulet[1], E. Benoit[1], E. Bernard[1], J.M. Bernard[1], M. Bernert[8], N. Bertelli[9], E. Bertrand[1], P. Beyer[3], J. Bielecki[10], P. Bienvenu[1], R. Bisson[3], B. Bliewert[8], G. Bodner[9], S. Bose[9], C. Bottereau[1], C. Bouchand[1], Y. Boumendjel[1], F. Bouquey[1], C. Bourdelle[1], J. Bourg[1], S. Brezinsek[11], F. Brochard[12], C. Brun[1], V. Bruno[1], H. Bufferand[1], A. Bureau[1], S. Burles[1], Y. Camenen[3], B. Cantone[1], E. Caprin[1], M. Carole[1], S. Carpentier-Chouchana[13], G. Caulier[1], F. Causa[14], N. Cazanave[1], N. Chanet[1], O. Chellai[9], Y. Chen[7], M. Chernyshova[15], P. Chmielewski[15], W. Choe[16], A. Chomiczewska[15], G. Ciraolo[1], F. Clairet[1], J. Coenen[11], L. Colas[1], G. Colledani[1], J. Colnel[1], P. Coquillat[1], E. Corbel[1], Y. Corre[1], X. Courtois[1], T. Czarski[15], A. Da Ros[1], R. Daniel[17], J. Daumas[1], M. De Combarieu[1], P. De Vries[13], C. Dechelle[1], F. Deguara[1], R. Dejarnac[18], J.M. Delaplanche[1], L.F. Delgado-Aparicio[9], E. Delmas[1], L. Delpech[1], C. Desgranges[1], P. Devynck[1], J. Denis[3], S. Di Genova[19], R. Diab[6], A. Diallo[9], M. Diez[1], G. Dif-Pradalier[1], M. Dimitrova[18], R. Ding[20], T. Dittmar[11], L. Doceul[1], M. Domenes[1], D. Donovan[21], D. Douai[1], L. Dubus[1], N. Dumas[1], R. Dumont[1], F. Durand[1], A. Durif[1], F. Durodié[22], D. Elbeze[1], S. Ertmer[11], A. Escarguel[3], F. Escourbiac[13], B. Esposito[23], K. Ezato[24], F. Faisse[1], J.L. Farjon[1], N. Faure[1], N. Fedorczak[1], P. Fejoz[1], F. Felici[25], C. Fenzi-Bonizec[1], F. Ferlay[1], L. Ferrand[13], L. Fevre[12], M. Firdaouss[1], L. Fleury[1], D. Flouquet[1], T. Fonghetti[1], A. Gallo[1], X. Garbet[1], J. Garcia[1], J.L. Gardarein[2], L. Gargiulo[1], P. Garibaldi[1], S. Garitta[1], J. Gaspar[2], E. Gauthier[1], S. Gazzotti[1], F. Gely[1], J. Gerardin[1], G. Gervasini[14], E. Geulin[1], M. Geynet[1], P. Ghendrih[1], I. Giacalone[1], C. Gil[1], S. Ginoux[1], S. Girard[1], E. Giroux[1], G. Giruzzi[1], M. Goniche[1], V. Gorse[1], T. Gray[26], E. Grelier[1], C. Grisolia[1], A. Grosjean[21], A. Grosman[1], O. Grover[8], D. Guibert[1], D. Guilhem[1], C. Guillemaut[1], B. Guillermin[1], R. Guirlet[1], J.P. Gunn[1], Y. Gunsu[27], T. Gyergyek[28], S. Hacquin[1], A. Hakola[29], J. Harris[26], J.C. Hatchressian[1], W. Helou[13], P. Hennequin[30], C. Hernandez[1], L. Hijazi[1], J. Hillairet[1], T. Hirai[13], G.T. Hoang[1], C. Honoré[30], M. Houry[1], A. Huart[1], G. Huijsmans[1], P. Huynh[1], M. Iafrati[23], F. Imbeaux[1], N. Imbert[1], I. Ivanova-Stanik[15], P. Ivanova[31], R. Jalageas[1], A. Jamann[1], C. Jammes[1], A. Jardin[10], L. Jaubert[1], G. Jiolat[1], E. Joffrin[1], C. Johnson[26], A. Jonas[1], A. Kirschner[11], C.C. Klepper[26], M. Komm[18], M. Koubiti[3], S. Kosslow[21], J. Kovacic[28], M. Kozeiha[1], K. Krieger[8], K. Krol[10], I. Kudashev[19], B. Lacroix[1], L. Laguardia[14], V. Lamaison[1], V. Lapleigne[1], H. Laqua[31], C. Lau[28], Y. Lausenaz[1], R. Lé[1], M. Le Bohec[1], N. Lefevre[1], N. Lemoine[12], E. Lerche[22], Y. Lesourd[1], L. Letellier[1], M. Lewerentz[32], Y. Li[11], A. Liang[7], P. Linczuk[33], C. Linsmeier[11], M. Lipa[1], X. Litaudon[1], X. Liu[7], J. Llorens[1],

T. Loarer[1], **A. Loarte**[13], **T. Loewenhoff**[11], **G. Lombard**[1], **J. Lore**[26], **P. Lorenzetto**[34], **B. Lu**[7], **A. Lumsdaine**[26], **R. Lunsford**[9], **T. Lunt**[8], **G. Luo**[20], **P. Magaud**[1], **P. Maget**[1], **J.F. Mahieu**[1], **P. Maini**[1], **P. Malard**[1], **K. Malinowski**[15], **P. Manas**[1], **L. Manenc**[1], **V. Maquet**[22], **Y. Marandet**[3], **C. Martin**[3], **E.J. Martin**[26], **P. Martino**[1], **M. Mayer**[8], **D. Mazon**[1], **S. Mazzi**[1], **P. Messina**[1], **L. Meunier**[1], **D. Midou**[1], **G. Miglionico**[1], **Y. Mineo**[1], **M. Missirlian**[1], **R. Mitteau**[1], **B. Mitu**[35], **D. Moiraf**[1], **P. Mollard**[1], **G. Momparler**[1], **V. Moncada**[1], **T. Mondiere**[1], **C. Monti**[23], **J. Morales**[1], **M. Moreau**[1], **Ph. Moreau**[1], **Y. Moudden**[1], **G. Moureau**[1], **D. Mouyon**[1], **M. Muraglia**[3], **T. Nakano**[24], **E. Nardon**[1], **A. Neff**[26], **F. Nespoli**[9], **J. Nichols**[21], **L. Nicolas**[1], **S. Nicollet**[1], **R. Nouailletas**[1], **M. Ono**[9], **V. Ostuni**[1], **O. Paillat**[1], **C. Parish**[26], **H. Park**[36], **H. Parrat**[1], **J.Y. Pascal**[1], **B. Pegourie**[1], **F.P. Pellissier**[1], **Y. Peneliau**[1], **M. Peret**[1], **E. Pignoly**[1], **G. Pintsuk**[11], **R. Pitts**[13], **C. Pocheau**[1], **A. Podolnik**[18], **C. Portafaix**[1], **M. Poulos**[9], **P. Prochet**[1], **A. Puig Sitjes**[32], **R. Ragona**[37], **M. Rasinski**[11], **S. Ratynskaia**[38], **G. Raup**[8], **X. Regal-Mezin**[1], **C. Reux**[1], **J. Rice**[6], **M. Richou**[1], **F. Rigollet**[2], **N. Rivals**[1], **H. Roche**[1], **S. Rodrigues**[1], **J. Romazanov**[11], **G. Ronchi**[26], **C. Ruset**[35], **R. Sabot**[1], **A. Saille**[1], **R. Sakamoto**[39], **B. Salamon**[1], **F. Samaille**[1], **A. Santagiustina**[1], **B. Santraine**[1], **Y. Sarazin**[1], **O. Sauter**[25], **Y. Savoie-Peysson**[1], **L. Schiesko**[1], **M. Scholz**[10], **J.L. Schwob**[40], **E. Serre**[19], **H. Shin**[16], **S. Shiraiwa**[9], **Ja. Signoret**[1], **O. Skalli-Fettachi**[1], **P. Sogorb**[1], **Y. Song**[20], **A. Spring**[32], **P. Spuig**[1], **S. Sridhar**[1], **B. Stratton**[9], **C. Talatizi**[1], **P. Tamain**[1], **R. Tatali**[19], **Q. Tichit**[1], **A. Torre**[1], **L. Toulouse**[1], **W. Treutterer**[8], **E. Tsitrone**[1], **E.A. Unterberg**[26], **G. Urbanczyk**[12], **G. Van Rooij**[41], **N. Varadarajan**[1], **S. Vartanian**[1], **E. Velly**[1], **J.M. Verger**[1], **L. Vermare**[30], **D. Vezinet**[1], **N. Vignal**[1], **B. Vincent**[1], **S. Vives**[1], **D. Volpe**[1], **G. Wallace**[6], **E. Wang**[11], **L. Wang**[20], **Y. Wang**[7], **Y.S. Wang**[20], **T. Wauters**[13], **D. Weldon**[1], **B. Wirth**[21], **M. Wirtz**[11], **A. Wojenski**[33], **M. Xu**[7], **Q.X. Yang**[20], **H. Yang**[1], **B. Zago**[1], **R. Zagorski**[15], **B. Zhang**[20], **X.J. Zhang**[20], **X.L. Zou**[1] and the EUROfusion Tokamak Exploitation Team**[b]**

[1] CEA, IRFM, F-13108 Saint Paul-lez-Durance, France
[2] Aix Marseille University, CNRS, IUSTI, F-13453 Marseille, France
[3] Aix Marseille University, CNRS, PIIM, F-13397 Marseille, France
[4] American University of Beirut, Riad el-Solh, Beirut 1107-2020, Lebanon
[5] Karlsruhe Institute of Technology, Institute for Applied Materials, Karlsruhe, Germany
[6] MIT Plasma Science and Fusion Center, Cambridge, MA 02139, United States of America
[7] Southwestern Institute of Physics, Chengdu 610041, China
[8] Max-Planck-Institut für Plasmaphysik, D-85748 Garching, Germany
[9] Plasma Physics Laboratory, Princeton University, PO Box 451, Princeton, NJ 08543, United States of America
[10] Institute of Nuclear Physics Polish Academy of Sciences (IFJ PAN), PL-31-342 Krakow, Poland
[11] Institut für Energie- und Klimaforschung—Plasmaphysik, Forschungszentrum Jülich GmbH, Jülich, Germany
[12] Institut Jean Lamour, Université de Lorraine, Vandoeuvre-lés-Nancy, 54000 Nancy, France
[13] ITER Organization, Route de Vinon-sur-Verdon, F-13067 St Paul Lez Durance Cedex, France
[14] IFP-CNR, via R. Cozzi 53, 20125 Milano, Italy
[15] Institute of Plasma Physics and Laser Microfusion, 23 Hery, 01-497 Warsaw, Poland
[16] Korea Advanced Institute of Science and Technology, Daejeon, Korea, Republic Of
[17] Institute for Plasma Research, Bhat, Gandhinagar, Gujarat, India
[18] Institute of Plasma Physics of the CAS, Za Slovankou 3, Prague 8 18200, Czech Republic
[19] Aix-Marseille University, CNRS, M2P2, F-13451 Marseille, France
[20] Institute of Plasma Physics, Chinese Academy of Sciences (ASIPP), Hefei, China
[21] University of Tennessee, Knoxville, TN 37996, United States of America
[22] LPP-ERM/KMS, TEC partner, Brussels, Belgium
[23] ENEA C. R. Frascati, via E. Fermi 45, 00044 Frascati (Roma), Italy
[24] National Institutes for Quantum and Radiological Science and Technology, Naka-shi, Japan
[25] EPFL, Swiss Plasma Center (SPC), CH-1015 Lausanne, Switzerland
[26] Oak Ridge National Laboratory, Oak Ridge, TN 37831-6169, United States of America
[27] Pohang University of Science and Technology, Pohang, Korea, Republic Of
[28] University of Ljubljana, Faculty of Electrical Engineering, Trzaska 25, 1000 Ljubljana, Slovenia
[29] VTT Technical Research Centre of Finland Ltd, PO Box 1000, FI-02044 VTT, Finland
[30] Ecole Polytechnique, LPP, CNRS UMR 7648, 91128 Palaiseau, France

[31] Bulgarian Academy of Sciences, 1784 Sofia, Bulgaria

[32] Max Planck Institute for Plasma Physics, Wendelsteinstrasse 1, 17491 Greifswald, Germany

[33] Warsaw University of Technology, Institute of Electronic Systems, Nowowiejska 15/19, 00-665 Warsaw, Poland

[34] Fusion for Energy, 08019 Barcelona, Spain

[35] National Institute for Laser, Plasma and Radiation Physics, 409 Atomistilor Street, Magurele 077125, Romania

[36] Ulsan National Institute of Science and Technology, Ulsan, Korea, Republic Of

[37] DTU, Technical University of Denmark, Lyngby, Denmark

[38] KTH, Royal Institute of Technology, SE-10044 Stockholm, Sweden

[39] National Institute for Fusion Science, NIFS, Toki, Gifu 509-5292, Japan

[40] Racah Institute of Physics, Hebrew University of Jerusalem, Jerusalem, Israel

[41] Dutch Institute for Fundamental Energy Research, De Zaale 20, 5612 AJ Eindhoven, Netherlands

E-mail: jerome.bucalossi@cea.fr

CrossMark

Abstract

The mission of WEST (tungsten-W Environment in Steady-state Tokamak) is to explore long pulse operation in a full tungsten (W) environment for preparing next-step fusion devices (ITER and DEMO) with a focus on testing the ITER actively cooled W divertor in tokamak conditions. Following the successful completion of phase 1 (2016–2021), phase 2 started in December 2022 with the lower divertor made entirely of actively cooled ITER-grade tungsten mono-blocks. A boronization prior the first plasma attempt allowed for a smooth startup with the new divertor. Despite the reduced operating window due to tungsten, rapid progress has been made in long pulse operation, resulting in discharges with a pulse length of 100 s and an injected energy of around 300 MJ per discharge. Plasma startup studies were carried out with equatorial boron nitride limiters to compare them with tungsten limiters, while Ion Cyclotron Resonance Heating assisted startup was attempted. High fluence operation in attached regime, which was the main thrust of the first campaigns, already showed the progressive build up of deposits and appearance of dust, impacting the plasma operation as the plasma fluence increased. In total, the cumulated injected energy during the first campaigns reached 43 GJ and the cumulated plasma time exceeded 5 h. Demonstration of controlled X-Point Radiator regime is also reported, opening a promising route for investigating plasma exhaust and plasma-wall interaction issues in more detached regime. This paper summarises the lessons learned from the manufacturing and the first operation of the ITER-grade divertor, describing the progress achieved in optimising operation in a full W environment with a focus on long pulse operation and plasma wall interaction.

Keywords: nuclear fusion, magnetic confinement, tokamak, divertor, WEST, ITER

(Some figures may appear in colour only in the online journal)

1. Introduction

The primary mission of the WEST tokamak is to explore long pulse operation in a full tungsten environment to prepare for next step fusion devices, such as ITER and DEMO. The WEST programme is in particular focussed on assessing the performance of the ITER actively cooled tungsten (W) divertor under tokamak operation in fully actively cooled W environment [1]. With phase 2 of the WEST project, the lower divertor is now fully equipped with ITER-grade actively cooled plasma facing units (PFUs) [2]. Figure 1 shows a view of WEST in the phase 2 configuration. The divertor ring consists of 456 PFUs, each

of them having 35 W mono-blocks. Each PFU reproduces the straight part of the vertical targets of the ITER divertor, corresponding to one third of the total length of the ITER PFU. A sketch comparing an ITER divertor cassette and a WEST divertor sector is shown in figure 2. WEST uses the same mono-block technology, the same geometrical shape of the mono-blocks (toroidal bevel) and the same thermohydraulic conditions as ITER. The WEST divertor contains 15 960 W mono-blocks, which represents 10% of the number of mono-blocks foreseen in the ITER divertor vertical targets. The manufacturing of the actively cooled W divertor of WEST, carried out by the Chinese company AT&M (Advanced Technology
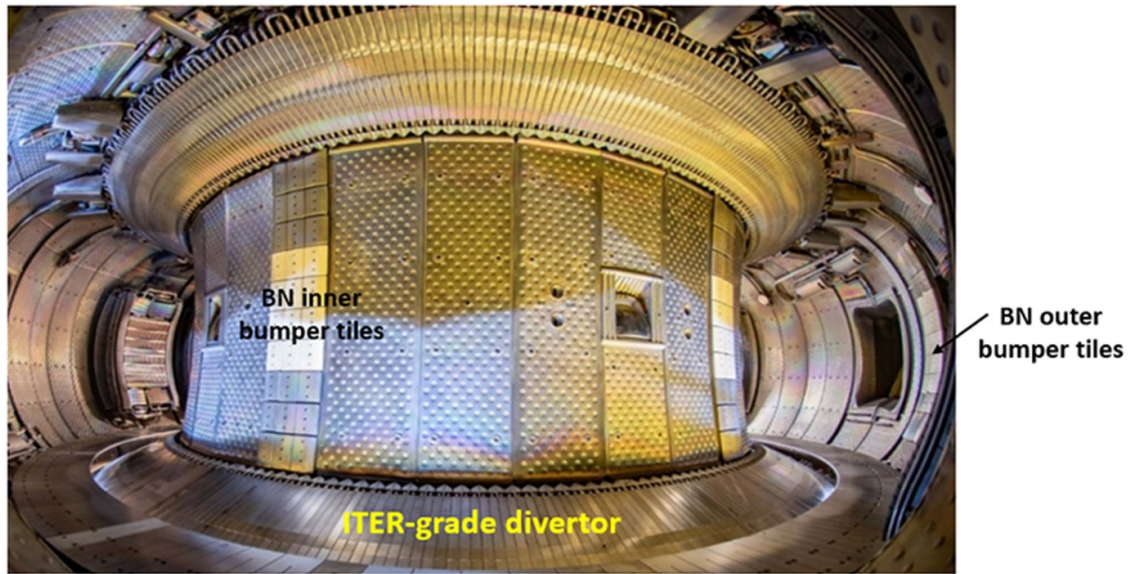
Figure 1. View of WEST in phase 2 configuration, with its full ITER-grade lower divertor, and boron nitride (BN) central tiles on the inner and outer bumpers.
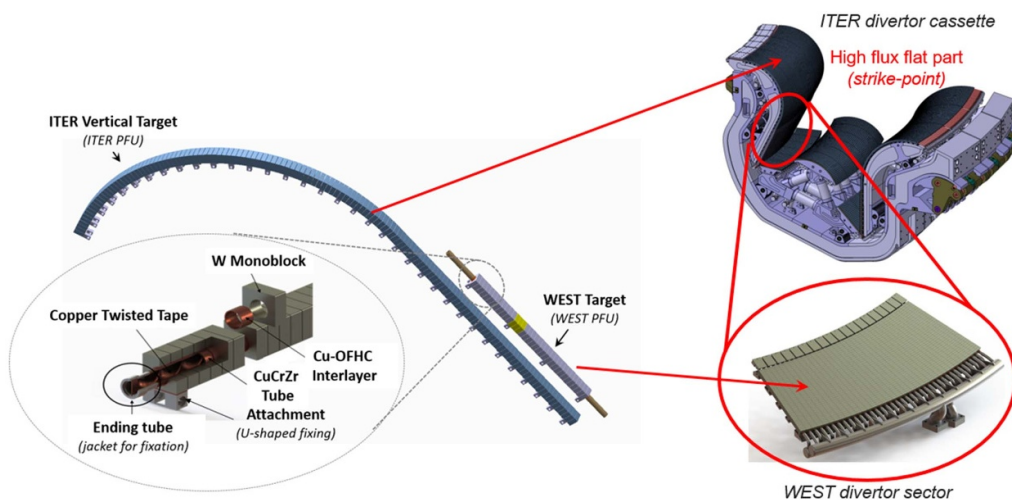

Figure 2. Comparison of an ITER divertor cassette and the WEST lower divertor. WEST uses the same mono-block technology, the same geometrical shape of the mono-blocks (toroidal bevel) and the same thermohydraulic conditions as ITER. Reprinted from [2], Copyright (2023), with permission from Elsevier.

of Materials), required for the first time a large scale industrial production of ITER-grade PFUs [3]. This allowed feedback on handling non-conformities and developing optimised reception tests [4], as required for the ITER divertor series production.

The WEST phase 2 configuration, with all its plasma facing components actively cooled, enables to run experiments with long plasma duration, relevant for testing the components under steady state conditions. Phase 2 began in December 2022 with only a few ohmic plasma discharges (C6 campaign). During the following campaign (C7), which ran from January 2023 to April 2023, rapid progress towards long pulse

operation was achieved, resulting in discharges of 100 s pulse length and injected energy of ∼300 MJ per discharge. In total, the cumulated injected energy during the campaign reached 43 GJ and the cumulated plasma time exceeded 5 h.

The paper is organised in three main parts: the first one reports on the manufacturing and qualification of the ITER grade divertor components and on imbedded diagnostics. The second part addresses scenario development progress with the actively cooled tungsten divertor towards long pulse operation. The last part focuses on plasma-wall interaction studies with the first effects of plasma exposure on tungsten divertor surface.

2. The full ITER grade divertor in WEST

2.1. Manufacturing and qualification of the ITER grade divertor

The production and the installation of the fully actively cooled ITER-grade PFUs for the WEST lower divertor (i.e. 456 PFUs in total) was successfully achieved at the end of 2021 [2, 3]. The WEST PFUs were manufactured by the Chinese company AT&M (Advanced Technology of Materials). This manufacturing was monitored by CEA/IRFM with the assistance of an expert team from ASIPP, China. This collaboration was instrumental in the production of these critical components, whose manufacturing process involve several critical steps. The quality assessment, through an extensive programme of reception tests and after a prior additional R&D phase to increase the reliability of the manufacturing, showed constant quality of the series production, both for the standard PFUs, as well as for the diagnostics PFUs. The reduced number of Non-Conformance Reports (NCRs) validated quite quickly the additional R&D carried out before launching the industrial production. In particular, the rejection rate decreased between the first months of production (June 2019) and the last ones (August 2020). This rejection rate was mainly dominated by issues during the Hot Isostatic Pressing (HIP) joining process. The rejection rate was significant during the first five months of the series production (higher than 50%). To make the upscaling of the manufacturing production more reliable, a more precise monitoring of both simultaneous applied temperatures and pressure, also by improving the canning and its welding, was implemented. This additional R&D phase enabled to reduce drastically the leakage during the HIP joining process and the defect issues at the material interfaces, and to reach a rejection rate close to 15% for the last ten months of the series production. Thereafter, cross-checking analysis was performed between Ultrasonic Testing (UT), performed by the manufacturer to control and measure the compliance of potential defects at interfaces, and tests by infrared (IR) thermography under high heat flux to assess the heat transfer capability. A few mono-blocks (less than 2%, but impacting about 8% of the total series production) declared compliant after UT had thermal defects seen by thermographic examination.

Subsequently, all thermal imperfections revealed only by thermographic examination were systematically tested under High Heat Flux and exhibited abnormal overheating at 10 MW m^{-2} (nominal heat load conditions) without any sign of propagation after 100 cycles. However, an attempt to cycle at a higher heat flux (up to 15 MW m^{-2}) showed a rapid increase in the surface temperature (from $\sim$10% to $\sim$20% after only ten cycles) suggesting a progressive degradation of the heat removal capacity of these PFUs due to the heat load cycles. In conclusion, the IR thermography analysis performed after delivery during the reception test at CEA Cadarache, in addition to the UT performed by the manufacturer during the manufacturing process, reveals to be a useful complementary non-destructive functional control technique to assess the heat transfer capability of the completed PFUs.

2.2. Embedded diagnostics

With phase 2 of WEST, the divertor has become a testbed for embedded diagnostics in ITER-grade PFUs to monitor relevant plasma and operational parameters, based on thermal sensors and Langmuir probe technologies. Innovative concepts have been developed to comply with the integration constraints associated to the ITER-grade technology and its assembly on the divertor structure. These diagnostics have been successfully tested during the C7 experimental campaign. The temperature in the ITER-grade components is monitored using embedded thermocouples and multiplexed Fibre Bragg Gratings (FBG) sensing probes, located 5 mm below the top surface of the mono-block and deployed in the maximum heat flux areas, on the inner and outer sides of the divertor. 16 thermocouples have been installed into two PFUs, whereas multiplexed FBGs have been embedded into five PFUs, providing 14 spot temperature measurement points per probe (i.e. 86 spot temperature measurement points in total including both TCs and FBGs) [5]. Thermal inversion of the sensor measurements allows to derive the heat flux distribution (peak heat flux and heat flux decay length λ_q) as function of time [6]. Measurements of the local plasma parameters, such as electron temperature, density and floating potential, from which the heat load can be derived, are provided by Langmuir probes [7]. Ten PFUs are equipped with Langmuir probes (56 probes in total) that are located in the vicinity of the separatrix strike points on the divertor target to characterise the plasma parameters, in particular the particle fluence during long pulse operation. In addition, 60 Langmuir probes are installed in the upper divertor.

3. Plasma scenario development and long pulse operation

3.1. Advances in long pulse operation

The results obtained during the first experimental campaigns of phase 2 include discharge lasting 100 s with $\sim$300 MJ of injected energy, and repetitive discharges lasting more than a minute for the high fluence programme. Overall, cumulated injected energy of 43 GJ and cumulative plasma time of over 5 h were achieved. These results are comparable to the energy values accumulated in Tore Supra in 2007–2008, where significant progress was achieved in the field of steady-state tokamak research (plasma times of 10 h in both 2006 and 2007, with 65 GJ injected RF energy in 2006 and 40 GJ in 2007) [8]. The plasma exposure achieved in WEST is, up to now, mainly characterised by stationary plasma conditions in the L-mode regime with attached divertor plasma conditions. The electron temperature (T_e), as measured from Langmuir probes embedded in the divertor, lies between 20 and 40 eV at the strike point on both inner and outer legs of the divertor. In/out asymmetries are observed, which can vary depending on the plasma conditions (see [9, 10] for more detailed discussion on heat flux and particle flux divertor asymmetries, respectively).
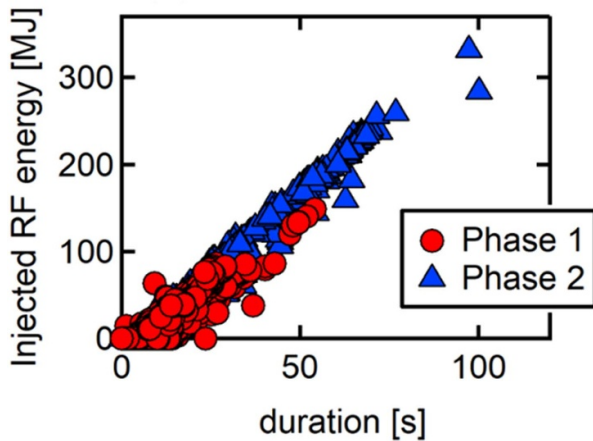
Figure 3. Pulse duration as a function of additional power achieved in WEST phase 1 (circles) and phase 2 (triangles). Reproduced with permission from [13]. CC BY-NC-ND 4.0.

Figure 4. Example of 100 s long discharge in WEST phase 2.

The progress made in term of long pulse operation (plasma duration and injected RF energy) is displayed in figure 3. Discharges of 100 s duration have been obtained in the recent campaign. Long plasma durations are obtained thanks to the non-inductive current drive capability from the Lower Hybrid Current Drive (LHCD) system. The current two RF heating systems of WEST, i.e. LHCD and Ion Cyclotron Resonance Heating (ICRH), provide torque-free and dominant electron heating that is adapted for developing ITER and DEMO relevant plasma scenarios, but are challenging to use in a tungsten wall tokamak. In particular, the amount of tungsten present in the plasma affects the current density profile build up and its evolution, making the development of a stable LH driven scenario difficult and time consuming. Consequently, the pulse length could be limited by several factors: MHD stability (evolution of the plasma current profile), flux consumption limit (a stable fully non-inductive scenario has not been yet developed), heating system failure (arcing, trips), impurity influx (so-called 'UFOs'), and plasma facing component overheating. The limitation in pulse length in discharge #57757, displayed in figure 4, was due to a real-time security on the IR temperature survey of the upper divertor area, where the fast electron from LHCD trapped in the ripple of the toroidal field are drifting to. Post-pulse analysis showed that the region of interest used also included a reflection from a tungsten inertial protection plate, which has not reached equilibrium conditions and whose temperature limit is much higher than that of the cooling pipe. The safety trigger was therefore inappropriate. The reflection zone has been carefully excluded from the region of interest for the next campaign. It has to be noted that the maximum cooling pipe temperature can be a limitation when going to lower densities required for fully non inductive operation. This limitation led to a thorough campaign of measurement of the emissivity of the pipes that is instrumental for infering the real temperature in a metallic environment [11, 12]. After this new evaluation, the apparent temperature limit on the cooling pipe has been increased and the operational
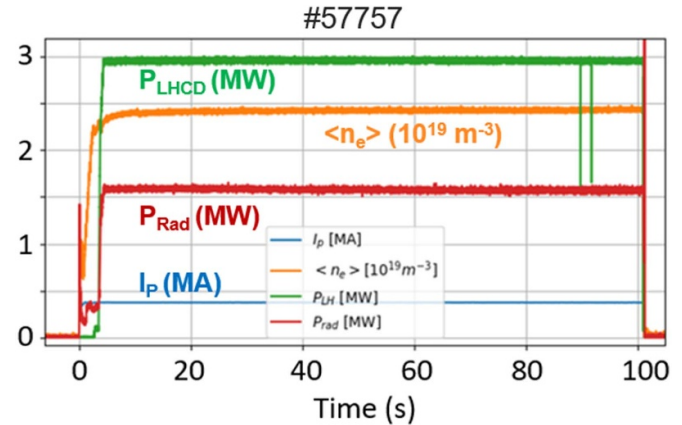
margins for long pulse operation are extended for the next campaign.

3.2. Conditioning of the ITER-grade divertor

The radiated power fraction in WEST standard L-mode plasmas with RF heating (LHCD or ICRH) is typically ∼50% [14, 15]. The radiated power fraction can be reduced to 20%–30% after a fresh boronisation, but this effect only lasts for a few pulses [15]. Boronisation has been employed with different intervals since the start of WEST operation (see figure 5). Only two boronisations have been carried out in phase 2 so far. After the installation of the full actively cooled ITER-grade divertor and pump-down, the vacuum vessel was baked between 90 °C and 170 °C for approximately two weeks. After 82 h at 90 °C and 33 h at 170 °C, the vacuum conditions were stable with a vessel pressure of 6×10^{-5} Pa and mass spectra dominated by H_2 molecules. Three sessions of D_2 glow discharge cleaning (GDC), for a total of 40 h, was then carried out at 170 °C. The first boronisation was then carried out for five hours, using a mix of 15% B_2D_6 and 85% helium and a total boron mass of ∼12 g. It has to be noted that this boronisation was carried out at 170 °C, a higher temperature than used during phase 1 (typically 90 °C). Once back at the operating temperature of 70 °C, the pressure in the vessel was 5.5×10^{-6} Pa and the plasma restarted smoothly with a cumulative plasma time of ∼30 s over the initial five pulses, showing that the conditioning of the new ITER-grade divertor was successful.

Figure 5 shows the evolution of the oxygen content in the ohmic phase of the plasma along the campaigns, represented by the oxygen-V line intensity normalised to the central line integrated density. A decrease in oxygen content can be seen immediately after the boronisations, followed by an increase during the subsequent plasma operations with different dynamics. A high fluence campaign was carried out in March–April 2023 (section 4.4), characterised by repetitive discharges in an identical plasma scenario. No further boronisation was carried out after the start of the high fluence campaign in order to assess the evolution of the conditioning effect of a boronisation. Saturation was observed after around
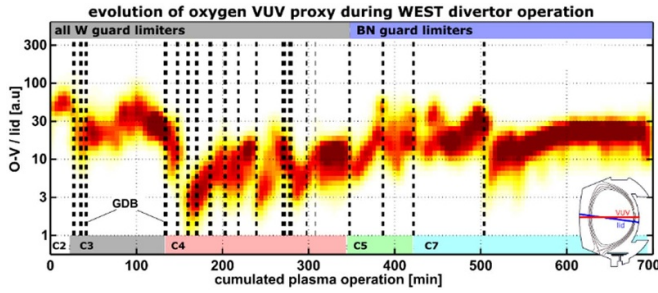
Figure 5. Oxygen line intensity normalised to central line integrated density for all discharges in WEST as a function of cumulated plasma time. A decrease in oxygen level can be seen after the boronisations.

Figure 6. Time evolution of the radiated power fraction during the plasma start-up phase with W limiters and BN limiters. The dotted line is the averaged radiated power fraction obtained with W limiters and the shaded area the distribution of the pulses with W limiters. The blue/red trace corresponds to a pulse with an early/late X-point formation with BN limiters.

Figure 7. Radiated power in the ohmic limiter phase during all campaigns in WEST.

100 min of plasma operation, with no further degradation in the following 100 min.

3.3. Plasma start up in tungsten environment

Efforts to develop robust plasma scenarios, conciliating edge and core plasma constraints in a full W environment, have been pursued in phase 2. Concerning the plasma start-up phase, WEST has been temporarily equipped with boron nitride (BN) tiles on the central part on the outer and inner bumpers (guard limiters) since the last campaign of phase 1 (see figure 1). The aim is to compare the plasma start-up behaviour with low-Z (BN) and high Z (W) first wall tiles. Figure 6 shows the time evolution of the radiated power fraction, defined as the radiated power in divertor plus bulk plasma divided by the heating power, during the first seconds of the discharge (only ohmic power in this phase), comparing the behaviour with W tiles and BN tiles on the equatorial limiters. The dashed black line represents the average of the radiated power fraction obtained with W tiles. The blue and red lines show two pulses with BN tiles with different timing of the X-point formation to a lower single null (LSN) plasma. As expected, the radiated power fraction is significantly lower during the limiter phase when using BN tiles and stable plasma conditions are more reliably obtained.

However, after 3 s, when the LSN plasma has been formed, the radiated power fraction reaches similar levels with W tiles and BN tiles. A careful analysis of the radiation level during the bouncing of the plasma in the early startup phase seems to indicate that the material of the outer limiter has a stronger impact on plasma contamination than the inner guard limiters. It is therefore important to have an accurate control of the plasma equilibrium during the plasma start-up phase in order to avoid contact with the outer limiter. The material on the inner guard limiters seems to play little role in the plasma contamination compared to the outer limiter.

Figure 7 shows the radiated power in the ohmic limiter phase for all the experimental campaigns, showing the change to BN limiters for the C5 campaign, which resulted in a significant decrease in radiated power at the start of C5. The vertical dashed lines indicate the boronisations that were performed more or less frequently during the different campaigns. It can be seen that the boronisation, by reducing oxygen/impurities
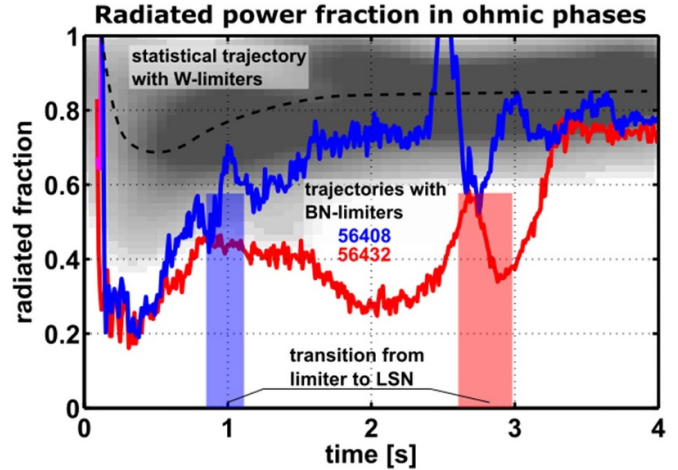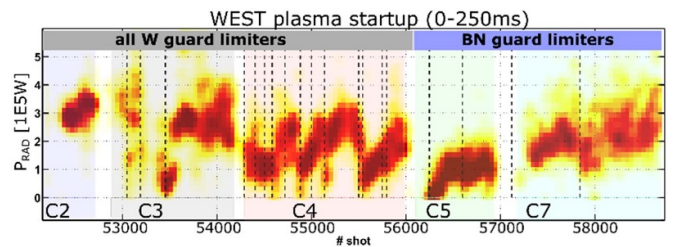
content and W sputtering, has a strong effect on start-up conditions, with an impact that lasts longer or shorter depending on the vacuum quality and subsequent plasma operations. It can also be seen that the radiated power towards the end of the C7 campaign is comparable to that during the first campaigns when W limiters were used. This could possibly be due to the build-up of deposited layers on the limiters, as well as on the lower divertor, as shown in section 4.4. Concerning the BN limiters tiles, they were indeed found to have a dark coloured deposit mainly composed of W after the C7 campaign.

Finally, promising results have been achieved with ICRH assisted breakdown in order to assess plasma breakdown at ITER relevant loop voltage ($E_{loop} \sim 0.3$ V m^{-1}). Plasma breakdown has so far been achieved at $E_{loop} \sim 0.5$ V m^{-1}, using 100 kW of ICRH power. Further experiments are planned to approach the ITER conditions.

3.4. Tungsten sources

The W contamination leads to $\sim$50% radiated power fraction in standard attached WEST plasma discharges [15], independently of the power coupled to the plasma or the heating mix used. Investigating the physics behind this resilient value motivated strong efforts, both experimentally and
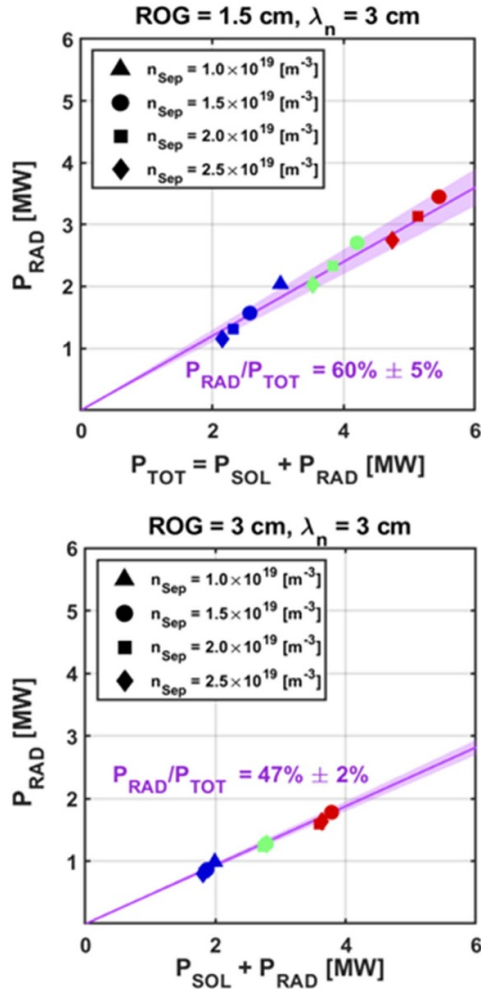
Figure 8. 3D transport simulations with SOLEDGE-ERO2.0 [16, 17] for two different radial outer gaps (ROG) between the RF antennas and the separatrix. Reproduced with permission from [17]. 29th IAEA Fusion Energy Conference (FEC 2023), Oct 2023, Londres, United Kingdom. ⟨cea-04566270⟩.

Figure 9. Experimental data of radiated power fraction in the bulk plasma for a series of 400 kA plasma discharges with 3–4 MW LHCD power. The scenario is described in section 4.4.

through modelling, given the constraints it imposes on present scenario developments and the extrapolation to ITER. In particular, tungsten contamination originating from passive RF antenna limiters (tungsten coated) has been investigated with ERO2.0, thanks to the new capability of the SOLEDGE code to handle non-axisymmetric objects [16, 17]. SOLEDGE 3D simulations were carried out to reproduce plasma main species (D and e) conditions, using a simple fluid model for neutrals and diffusive processes as a proxy for turbulent transport. ERO2.0 simulations were run to model W erosion and migration, adopting a 3% uniform concentration of oxygen to account for W sputtering by light impurities, in addition to W sputtering by D and W self-sputtering, to match the experimental radiation level. The impact of the proximity of the RF antenna limiters on the overall W content inside the separatrix has been investigated in the simulations. The results are shown in figure 8. The figure shows that the radiated fraction decreases as the radial outer gap
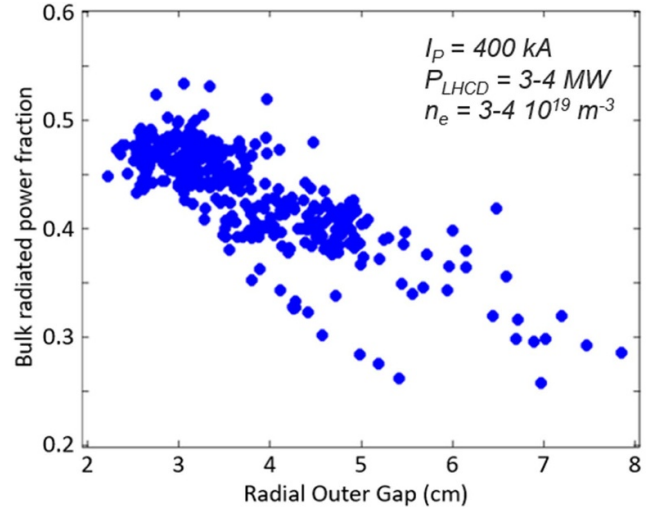
(ROG) between the RF antenna limiters and the separatrix increases, which is in agreement with the experimental results shown in figure 9. This suggests that it is essential to take into account toroidally localised objects to accurately simulate boundary phenomena and impurity physics in WEST discharges. Moreover, the distance between the RF antennas and the separatrix needs to be optimised for high power RF heating scenarios, in order to maintain the power coupled to the plasma while minimising impurity sources. This optimisation is particularly difficult when combining LHCD and ICRH systems, since they have different criteria for optimum coupling and different optimal antenna-separatrix distances.

Time-dependent simulations of the full discharge, including start-up and ramp-up phases, have also been performed with SOLEDGE 2D, thus allowing a quantitative evaluation of the W sputtering from the different plasma facing components to accurately treat the W source of contamination [18]. The experimental investigation of W erosion and contamination is supported by extensive visible spectroscopy lines of sight [19] viewing most in-vessel components, a bolometer system with 16 lines of sight [20], as well as UV spectroscopy allowing the identification of tungsten density profile [21]. These investigations allow identifying the different W sources activated by the two RF systems (LHCD and ICRH) [9, 14], although the radiated power fraction is comparable in both cases. SOLEDGE simulations indicate a substantial plasma-wall interaction in the upper divertor region, when the LSN magnetic configuration is used [17]. Indeed, the typical WEST LSN magnetic equilibrium used features a secondary X-point in the vicinity of the upper divertor, leading to significant W erosion in this area. Plasma interaction with the upper divertor while running in LSN has also been confirmed by energy balance measurements via calorimetry (section 4.1).
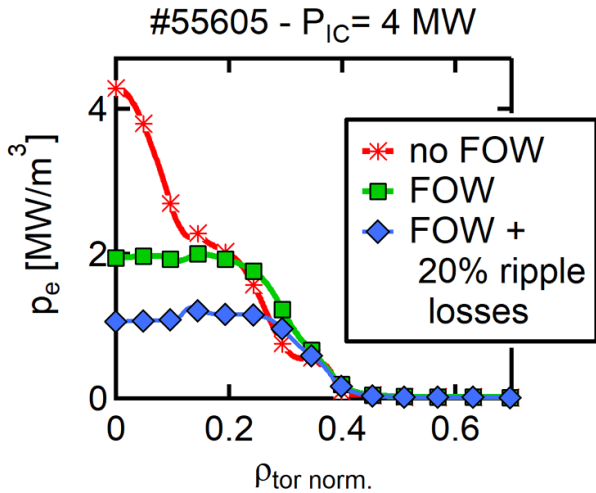
Figure 10. Electron heat source profile for 4 MW of ICRH power, with and without Finite Orbit Width (FOW) effects, and with 20% of total power loss in the ripple. Computations made with EVE [28] and AQL [29] with a surrogate model for FOW effects and fast ion energy truncation for ripple losses. Reproduced from [25]. © IOP Publishing Ltd. All rights reserved.

Figure 11. Ratio of the electron-ion heat exchange time over the energy confinement time, as a function of T_i/T_e, with points from the WEST database, and from METIS power and density scans. A 15 MA ITER case at $Q = 8$ is also shown. Reproduced from [36]. © 2024 The Author(s). Published by IOP Publishing Ltd on behalf of the IAEA. All rights reserved.

3.5. Core electron heating and confinement studies

The level of electron heating in the core is a crucial point for counteracting tungsten radiation and avoiding radiative collapse. Analysing these collapse events in LHCD or ICRH-heated plasmas gives key indications about the actual power deposition of both systems. For LHCD, it demonstrates that the hollowness of the deposition of the LHCD wave is getting more pronounced as the electron temperature decreases, leading eventually to a radiative collapse by the lack of core electron heating [15, 22, 23]. For ICRH, the spreading of the heat deposition by Finite Orbit Width (FOW) effects can reduce the electron heat source by a factor of two. In addition, the power loss associated to fast minority ions trapped in the ripple impacts essentially the electron heat source: with only 20% of total loss power (as quantified by IR measurements [24]) the electron heat source in the core is decreased by another factor of two [25] (see figure 10). The optimisation of the scenario taking into account these constraints points towards operating ICRH at large density to limit ripple losses [24], while the LHCD power should be scaled with plasma density to get a core absorption of the wave and remain in a 'hot branch' regime where the tungsten radiation decreases with increasing temperature [26]. The installation of the 3 MW Electron Cyclotron Resonance Heating (ECRH) system on WEST [27] will be instrumental in improving the core electron heating and consolidating the plasma scenarios.

Core tungsten peaking, determined from bolometer inversion, compares well with neoclassical prediction in LHCD heated plasmas [22], while for ICRH discharges a finite toroidal rotation is required to match the measurements, in agreement with the observed acceleration of MHD modes at the plasma edge [25]. Tungsten accumulation is only triggered when a radiative collapse is occuring, and it is then consistent
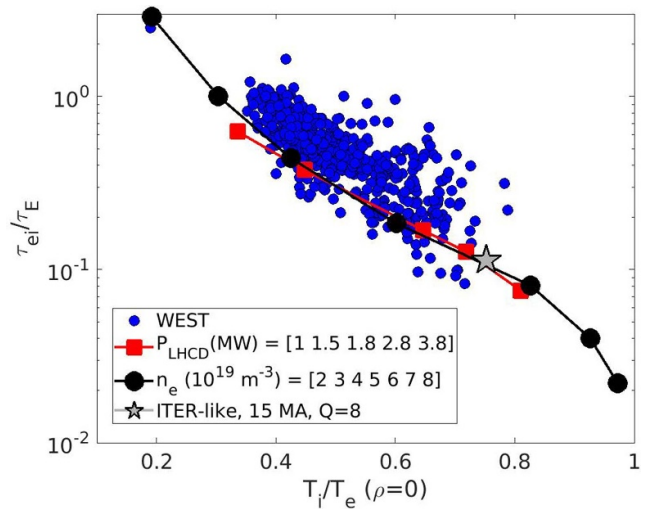
with the reduction or even reversal of the ion temperature screening effect [25].

The physics studies for characterising plasma scenarios in WEST highlight several key features of interest for ITER and DEMO. A strong correlation between core performance and separatrix quantities in L-mode is observed: high core energy and particle confinement are associated with low separatrix density [30]. Similar observations are reported for H-mode discharges in ASDEX Upgrade [31] and JET [32]. Understanding the mechanisms at play is essential for guiding extrapolations to large tokamaks, as these observations favour a low neutral recycling in present day devices. However, in ITER and beyond, the fuelling mechanism will be different due to higher opacity, requiring pellet fuelling. It is therefore essential to disentangle the casualty chain between core confinement, separatrix parameters and fuelling. A second topic is the mechanism of ion temperature saturation in electron-heated plasmas. This observation applies to the plasmas of WEST, as well as to other magnetic confinement devices [33], and results from the competition between the confinement time and the equipartition time. A self-consistent determination of the steady-state operation point, based on the combination of the METIS code [34] with the Neural Network regression of the reduced, quasilinear gyro-kinetic code QuaLiKiz [35], has been used on WEST parameters to validate the method. The ratio between ion and electron temperature tends to unity as the energy confinement time becomes larger than the equipartition time, as shown in figure 11. The simulation results for a density and a power scan match the WEST database, and the application to an ITER-like case at 15 MA with 50 MW of input power (NBI and ICRH) and an amplification factor $Q = 8$ follows the same line. This work gives confidence that dominant electron heating will not prevent high ion temperature and fusion performance in large tokamaks [36].
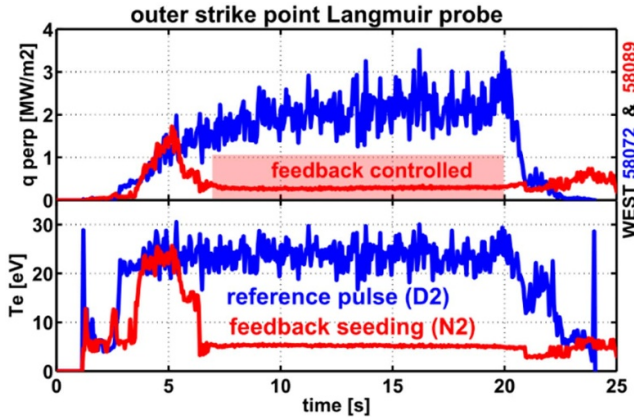
Figure 12. X-point radiator (XPR) experiment in WEST with feedback control using nitrogen injection.

Figure 13. Visible camera images showing the nitrogen injection location and the X-point radiator (XPR) phase.

3.6. Improved confinement with impurity seeding

Impurity seeding with nitrogen has been employed in WEST, first during the plasma current ramp-up phase in the phase 1 campaigns with W tiles on the inner and outer bumpers to improve plasma stability during the early ohmic phase [37], but recently also during the auxiliary heating phase in X-point plasmas. Using nitrogen seeding during the X-point phase, an X-Point Radiator (XPR) regime, as also obtained in ASDEX Upgrade [38] and JET [39], was achieved and maintained for 18 s. As seen in figure 12, the electron temperature and the heat load on the divertor target were reduced significantly when the XPR-phase was triggered and a radiating belt above the lower divertor is clearly visible (figure 13). The XPR-phase could be maintained and controlled in real-time using nitrogen injection at the outer midplane as an actuator and an interferometry line crossing the X-point as a sensor. In these experiments, both the energy confinement time and the neutron rate increased with the increase of the effective ion charge (Z_{eff}), as shown in figure 14, and the tungsten contamination was reduced. During these nitrogen seeded XPR plasmas, more peaked density profiles are observed, while the W density profile becomes less peaked. The integrated modelling work carried out so far suggests that two mechanisms are at play: firstly, reduced W peaking in the core due to enhanced neoclassical diffusion leads to larger electron temperature and, secondly, reduced ion heat turbulent transport (ITG stabilization due to dilution) leads to larger ion temperature. This XPR regime has been accessed in L-mode so far, and it opens a promising route for the development of a power plant-compatible scenario, and for the test of the ITER-grade PFUs in conditions where their lifetime should be extended.

In addition to nitrogen seeding, encouraging results have been obtained using boron injection from an Impurity Powder Dropper (IPD), with beneficial effects on both machine conditioning and core plasma performance [40–42]. The material introduced by the IPD is deposited onto the plasma-facing components through plasma-enhanced chemical vapour deposition. The drop rate was varied over the shot series and
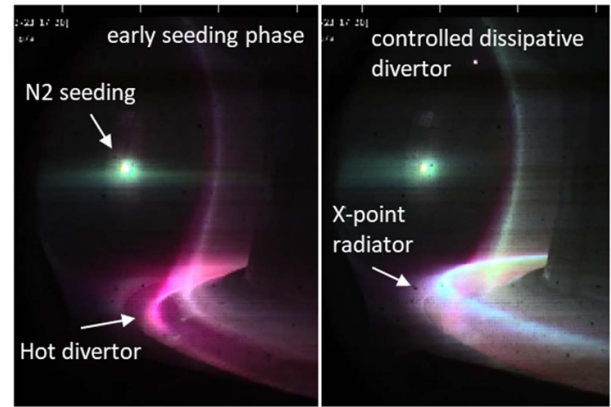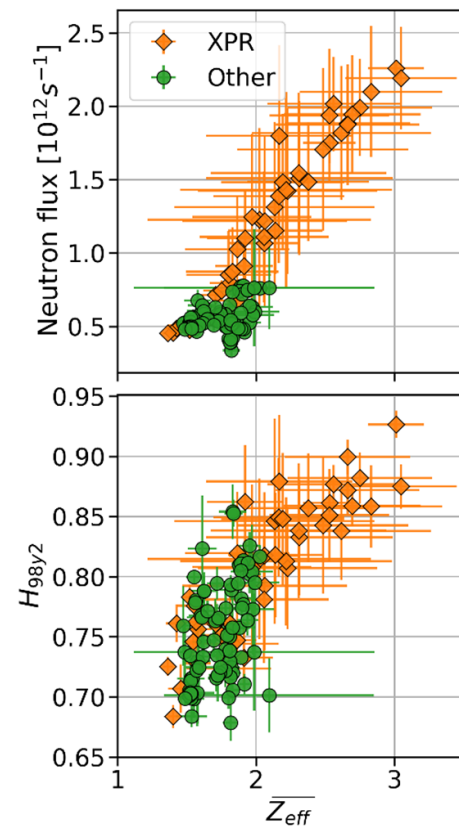

Figure 14. Neutron flux (left) and H98y,2 factor (right) as a function of the mean effective charge of the plasma in standard and XPR experiments.

an optimal powder injection rate was determined whereby disruption-free operation could be assured. Injection of boron powder resulted in a prompt increase in the stored energy (W_{MHD}) by up to 20% and in the measured neutron rate [42], similar to what was observed with nitrogen seeding. The increase is observed to persist for the entire duration of the powder injection. During the boron injection, the W_{MHD} was observed to increase proportionally to the decrease in overall deuterium recycling (determined by the reduction in the D_{γ}

signal normalized to the edge electron density). Reductions in edge neutral density have been previously associated with improved overall plasma performance [43, 44] and may serve as a channel for enhanced fuel dilution. In addition, during these injections, a positive impact was noted on the vessel wall conditions. Specifically, a reduction on the order of 40%–60% was observed in the D-I, O-II, C-II, and N-II line intensities at both the lower outer divertor, as well as at the RF antenna limiters. Reduced scrape-off layer (SOL) particle fluxes confirm these spectroscopic trends. Discharges following powder injection exhibited a decrease in low-Z impurity particle flux as well as W particle flux and reduced total radiated power.

4. Plasma wall interaction studies

4.1. Energy balance measurements via calorimetry

The WEST tokamak is perfectly suited to perform accurate and reliable energy balance measurements [45], due to its long pulse capability and thanks to the wide coverage of the water calorimetry sensors (94 thermal measurements and 72 flowmeters). The distribution of energy on the in-vessel components in the entire tokamak has been determined. A database of more than 600 pulses has been analysed, for each pulse the energy deposited has been measured with the water calorimetry system for the actively cooled components and with embedded thermocouples for the inertial components used in phase 1 [46]. The complementarity of these two thermal diagnostics allowed to close the energy balance between the measured energy and the injected energy with a difference of only 5% in most pulses and for all magnetic configurations. The plasma facing component that receives the highest fraction of energy is always the Outer First Wall (with about 30%), which is due to the large surface and the high radiated power fraction [14, 15]. The second kind of component receiving a high fraction of the injected energy are the lower and upper divertor, in LSN and USN configuration, respectively. It should be noted that when running in LSN, the lower divertor/upper divertor receive typically 25% and 10% respectively, while running in USN, the lower divertor/upper divertor receive typically 6% and 29% respectively, despite the lower and upper divertor being up-down symmetric. This is consistent with the fact that the lower divertor is equipped with a pumping baffle and that the USN configuration used has a larger clearance to the lower divertor, compared to the clearance of the LSN to the upper divertor. In addition, the information provided by the calorimetry system on the loads on first wall components (in particular the outboard limiter and the RF antenna limiters) could bring valuable insight on the far scrape-off layer through specific experiments using varying gaps between the plasma boundary and the first wall components.

4.2. Tungsten emissivity evolution from infrared measurements

WEST experiments have shown that the emissivity of metallic targets changes after plasma irradiation, mainly due to the erosion/deposition phenomenon that occurs during the plasma facing component lifetime [47]. A challenge for getting more reliable IR measurement and safe operation is therefore to be able to follow emissivity change during the experimental campaigns [11, 12]. Figure 15 shows the evolution of tungsten emissivity along an ITER-grade PFU after the C7 WEST campaign. The green area in figure 15 corresponds to the emissivity measured before plasma exposure on 25 ITER-grade PFUs, which was in the range between 0.07 and 0.2. The red curve in figure 15 shows the emissivity as measured along one PFU after the C7 campaign. On the inner and outer strike point areas, where erosion occurs, the emissivity falls to 0.05 close to polished pure W value. On the redeposition areas, where material accumulate, valued up to 0.85 were measured. For monitoring purposes, as well as for experimental studies, it is therefore essential to take into account this evolution of emissivity in order to control the measurement of the actual surface temperature.

From the IR synthetic diagnostic, inversion algorithms have been developed in order to retrieve surface temperature and/or emissivity from experimental images. A novel method has been investigated based on the supervised deep fully convolutional neural network [12]. Supervised deep-learning methods have been made on a big-data training set that enables to calibrate the weights of the neural networks. Such a method could be used to assess the emissivity of the WEST W divertor, making use of a baking period where the temperature of the divertor and the first wall are different and spatially uniform, in order to assess and monitor the emissivity. Experiments to validate this method could be performed in a future campaign if two different baking temperatures are used simultaneously, one for the divertor and one for the first wall.

4.3. Results on material migration and PFU testing

Several erosion marker tiles were implemented on the lower divertor to assess material migration during phase 1 of WEST [48]. They were retrieved for post mortem analysis throughout phase 1, which included five experimental campaigns (C1–C5). The analysis of the erosion marker tiles have shown that net erosion is found for both the inner and outer strike point areas (ISP and OSP respectively), with a more pronounced erosion area around the OSP [49]. Thick deposited layers (> several μm) were found on the High Field Side (HFS). Thin deposition (few 100's of nm) was found further away on the HFS and the Low Field Side (LFS). It was found that the evolution of the W emissivity is correlated to the erosion/deposition pattern, with values close to pristine W in net erosion areas and significantly higher in deposition-dominated areas (see figure 15). The thick deposited layers on the HFS were found to grow from $\sim$10 μm after C3 up to more than 30 μm after C5. In addition to tungsten (W), boron (B), carbon (C) and oxygen (O) were found to be the main impurities present in the layers [49, 50]. This is consistent with results from divertor visible spectroscopy, where B, C and O were clearly evidenced during plasma operation in phase 1.
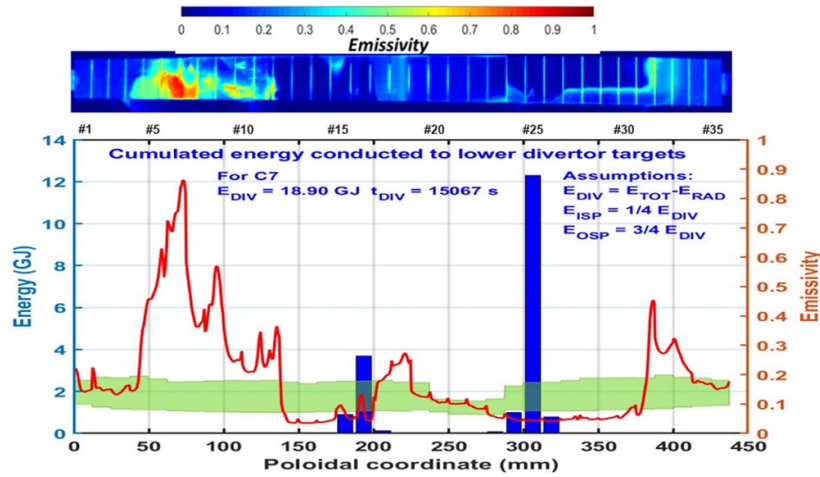
Figure 15. Laboratory measurement of emissivity before and after plasma exposure of a PFU following the C7 WEST campaign. The emissivity map of the PFU is shown at the top. The green area corresponds to the emissivity measured before plasma exposure. The red curve represents the emissivity after exposure. The histogram represents the energies deposited on the strike-points. The blue bars correspond to the location of the strike points (the high heat flux deposition and erosion area).
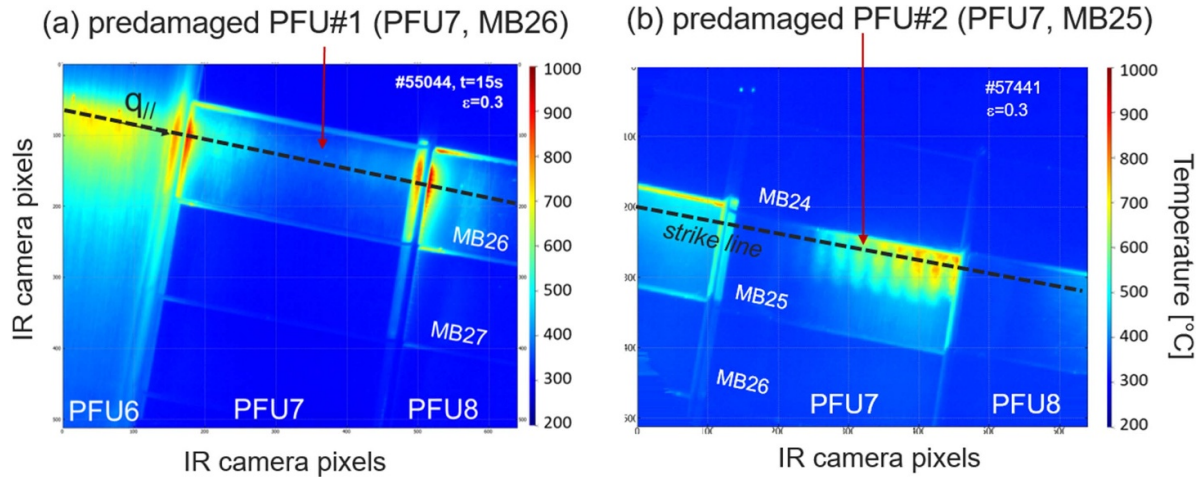

Figure 16. IR measurement of pre-damaged PFU#1 (crack network, unshaped geometry) exposed in C3-C4 and PFU#2 (crack network and melted droplet, shaped geometry) exposed in C7, assuming surface emissivity $\varepsilon = 0.3$. Reproduced with permission from [13]. CC BY-NC-ND 4.0.

Various W damage mechanisms have been identified on the PFU tested in phase 1 as a function of the heat loading exposure. For misaligned unshaped PFUs that were the first to be tested (PFU#1), regularly spaced cracking was observed on the leading edges [51]. A dedicated modelling tool (TREX code) [52] was developed to assess crack initiation under WEST conditions, showing that the observed crack pattern can be reproduced assuming brittle failure due to transients (600 MW m^{-2} during 3 ms disruptions).

Test of dedicated pre-damaged W mono-blocks have been carried out both during phase 1 and 2 to assess the impact of ELM-type damages on the heat exhaust of the PFUs as well as on plasma operation [13, 51]. Figure 16 shows IR measurements of pre-damaged PFU#1 (with crack network) exposed during C3-C4 campaigns (phase 1) and of pre-damaged PFU#2 (with crack network and melted droplet) exposed in C6-C7 (phase 2). The pre-damaged PFU#2, with more severe

type of damage (crack network and melted droplets), was exposed in phase 2 with the toroidal bevel geometry. The damaged mono-block was positioned in the high heat load area on a mono-block (#25), accessible with the standard magnetic configuration to maximise both thermal cycles and plasma exposure time. No significant degradation of the pre-damaged mono-block was observed after several hours of plasma exposure (pending detailed post mortem analysis). In addition, no impact on plasma operation (such as W flake ejection from the damaged area) was noticed. The W source emitted by a healthy versus the pre-damaged mono-block was measured by divertor visible spectroscopy with a line-of-sight viewing the mono-blocks and compared under similar plasma conditions. No noticeable difference was detected between the two mono-blocks WI emission, showing that the W sputtering was not affected by the surface morphology, such as roughness or cracks [13].

Surface analysis was then carried out on the pre-damaged mono-block PFU#2 following the C7 campaign, using a large-chamber scanning electron microscope [51]. It can be noted that the cracks that were visible on the pre-damaged area before the C7 campaign were now filled with deposits and a global smoothing of the surface was observed. The composition of the deposits seems to suggest the presence of Fe, Cu, Cr, C and O. These could be originating from other plasma facing components than the divertor (e.g. first wall, RF antennas), but further analysis are needed. The pre-damaged PFU#2 has been reinstalled in WEST for further plasma exposure in the coming experimental campaigns.

4.4. High fluence campaign

The last part of the C7 campaign in 2023 was devoted to a high fluence campaign in deuterium, with the goal to reach a ITER relevant cumulated divertor particle fluence exceeding an ITER discharge in the Pre-Fusion Plasma Operation phase. Repetitive discharges of ∼60 s pulse length were carried out during one month of operation, with the same plasma scenario illustrated in figure 17. The local divertor conditions in the most loaded area (outer strike point at the maximum toroidal location in the ripple modulated divertor pattern of WEST, see description in [9] and max OSP label in figure 21) corresponds to a heat load of 4 MW m^{-2} and electron temperature on the target of ∼25 eV. The inner strike point (max ISP label indicated in figure 21) shows an equivalent electron temperature but lower heat/particle fluxes (∼1 MW m^{-2}). The main plasma parameters were (as shown in figure 17): plasma current of 400 kA, line integrated density of 3.8×10^{19} m^{-2} and additional heating with 3.8 MW LHCD power. After four weeks of repeating the same plasma scenario, the cumulated particle fluence as measured from the divertor Langmuir probes reached a value of around 5×10^{26} D m^{-2} at the outer strike point (max OSP area). This corresponds to ∼2.5 nominal 200 s discharges in the ITER Pre-Fusion Plasma Operation phase, or ∼ 0.2 of a nominal ITER 400 s discharge in the nuclear phase, based on ITER fluence as given in [53]. Figure 18 shows the cumulated particle fluence (left scale) and individual shot fluence (right scale) as a function of the shot number during the High Fluence campaign. The variation of the individual shot fluence reflects the shot duration, with the highest shot fluence (∼4 10^{24} D m^{-2}) corresponding to the maximum shot duration achievable in the given plasma scenario (∼60 s as shown in figure 17).

It can be noted that no boronisation or boron powder injection was carried out during the last seven weeks of plasma operation of the C7 campaign, which corresponded to ∼200 min of plasma (see figure 5). The main reason was to avoid adding surface layers of boron on the PFUs before the post-mortem analysis of the PFUs. Therefore, only glow discharge cleaning was performed once or twice per week during the high fluence campaign to maintain reliable start-up conditions.

During the last two weeks of operation in the high fluence campaign, an increasing number of radiative events appeared, becoming significant once the cumulated injected energy had
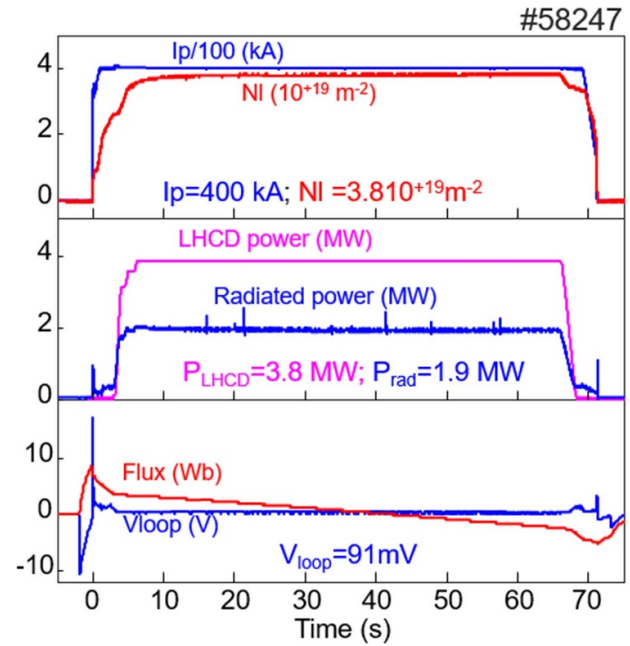

Figure 17. Plasma scenario used for the high fluence campaign at the end of the C7 experimental campaign.
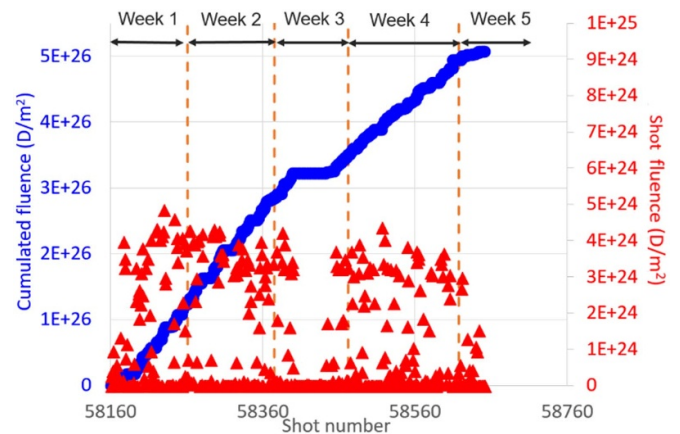

Figure 18. Deuterium fluence as a function of pulse number for the high fluence campaign.

reached ∼20 GJ since the start of the C7 campaign. A statistical analysis of the number of radiative events has been performed, based on bolometry. The radiative events investigated here are defined as an increase in radiated power of more than 250 kW compared to the base level of radiated power before the event. It shows that the radiative events occurred more frequently during the first 10 s of the discharge, in particular during the first few seconds after the application of the LHCD power.

Figure 19 shows a histogram of these radiative events ($\Delta P_{\rm rad} > 250$ kW), divided into three categories:

— Number of discharges which disrupted within 2 s and that were not associated with MHD activity;
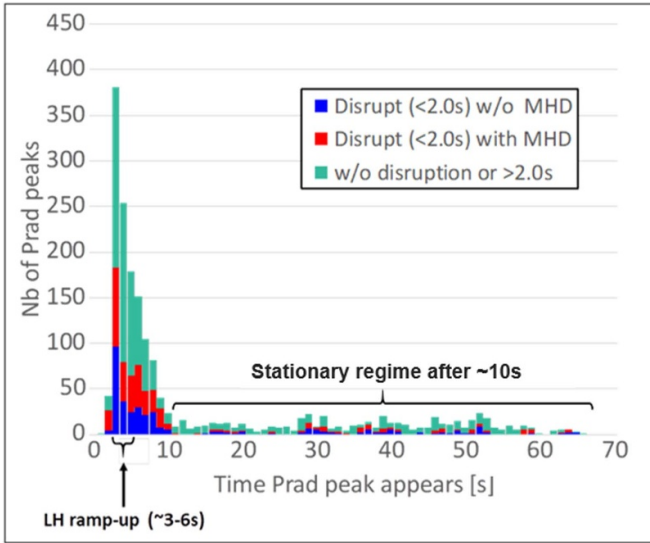— Number of discharges which disrupted within 2 s and that were associated with MHD activity;

Figure 19. Histogram of number of events with $\Delta P_{rad} > 250$ kW, divided into three categories as a function of the time when the radiated event appears during the discharge. Most of the radiative events and disruptions occurred during the first 10 s of the discharge.
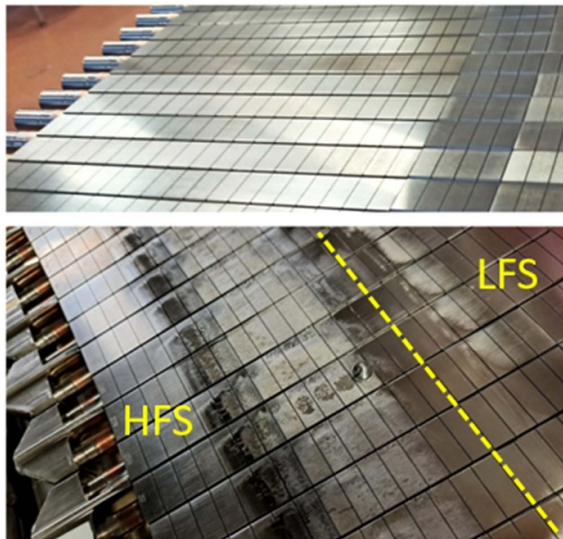

Figure 21. IR images of the ITER-grade divertor (top view, standard IR camera) in apparent temperature (assuming $\varepsilon = 1$) during the high fluence campaign, at the beginning (top) and end (bottom) of the campaign. The divertor heat load pattern is modulated toroidally by the magnetic field ripple (see [9] for more details).

Figure 20. Photos of the high field side of a divertor sector with ITER-grade W PFUs, before the C7 campaign (top) and after the campaign (bottom), showing presence of deposits on the high field side (HFS) of the inner strike point. The inner strike point is indicated by the dashed line.

Figure 22. Cumulated number of P_{rad} peaks ($\Delta P_{rad} > 250$ kW) against the cumulated plasma time during the high fluence campaign.

— Number of discharges which did not disrupt within 2 s after the radiative event.

Analysis of IR and visible camera images suggest that these radiative events are related to dust from deposits near the inner strike point on the lower divertor that enter the plasma and cause an increase in radiated power and, in some cases, disruption. Figure 20 shows photos of the high field side of the W-divertor, before (clean W surfaces) and after (presence of deposits) exposure in phase 2. IR cameras looking at the
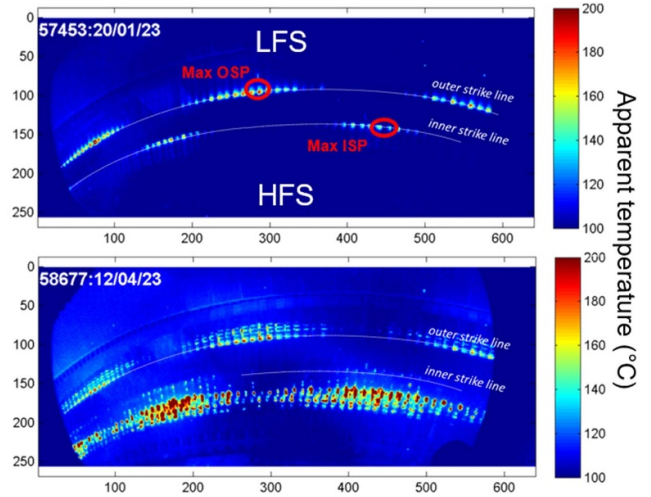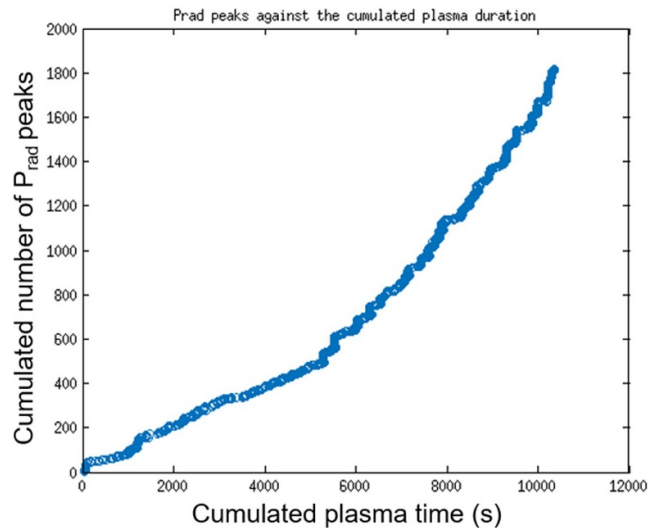
lower divertor (top view) have been used to monitor the evolution of the surface layers during the experimental campaign. Figure 21 shows two IR images taken before and at the end of the high fluence campaign, during the stationary phase of discharges having identical plasma parameters (LHCD power of 3.8 MW, $I_P = 400$ kA, $n_l = 3.8 \; 10^{19}$ m^{-2}). The inner and outer strike lines were clearly observed before the high fluence campaign (new ITER-grade components installed for phase 2). At the end of the high fluence campaign, the outer strike line is still visible while the inner strike line is barely visible. Hot surfaces attributed to surface layers are clearly visible beyond the inner strike point on the HFS.

Finally, figure 22 depicts the evolution of the cumulated number of radiative events ($\Delta P_{rad} > 250$ kW) during the high

fluence campaign, where identical shots were performed at injected power level of 3.8 MW. A break in the slope is visible after approximately 5500 s of plasma, which yields an approximate level of cumulated injected energy of ∼20 GJ. Cleaning of the HFS area of the divertor is currently planned before the next experimental campaign, in order to remove the deposits. Post-mortem analyses are now being carried out on selected PFUs to quantify the composition of the deposited layers.

5. Conclusion

The fully actively cooled ITER-grade divertor has been installed in the vacuum vessel of the WEST tokamak. This venture has provided useful experience in the large scale production of state-of-the-art components and a first feedback on the acceptance procedures planned for ITER procurements. The intensive tokamak operation that has begun in December 2022 with the ITER-grade divertor addressed both scenario and material aspects. Plasma current ramp-up performed on W or BN tiles during the limited phase showed similar radiative fraction in the diverted phase, demonstrating little legacy from one phase to the other. Tungsten tiles will be re-installed in 2024 for dedicated experiments focusing on the new ITER baseline constraints. Successful experiments of IC-assisted breakdown were performed and will be extended down to the available ITER loop voltage.

The resilience of the radiative fraction was documented both experimentally and through modelling, showing the role of the plasma-limiter distance and the light impurity concentration in the W contamination. At the same time, light impurity injection, either by gas puff or using the Impurity Powder Dropper, leads to improved core confinement with significant increase of the neutron rate. This is particularly examplified during the X-point radiator regime, where in addition tungsten sources from the divertor are largely suppressed.

The development of long pulse scenario lead to a first milestone of 100 s L-mode discharges in attached condition, and allowed to perform a first high fluence campaign in this plasma regime. A remarkable outcome of this campaign is the observation of a rapid build-up of deposits around the strike points and the generation of an increasing number of metallic clusters entering into the confined plasma. This suggests a key number for cumulated fluence equivalent to only one PFPO pulse before such events are observed in an attached regime in ITER, which could strongly reduce its capability to operate in attached reigme.

In summary, the first experiments carried out in WEST phase 2 open the path towards further long pulse operation campaigns at higher power and higher particle fluence under divertor conditions ranging from attached to detached regimes. These conditions are relevant for testing actively cooled plasma facing components for ITER and for carrying out plasma-wall interaction studies approaching fusion power plant long pulse constraints.

ORCID iD

A. Ekedahl ⬤ https://orcid.org/0000-0002-0376-5119

References

[1] Bucalossi J. *et al* 2022 *Nucl. Fusion* **62** 042007
[2] Missirlian M. *et al* 2023 *Fusion Eng. Des.* **193** 113683
[3] Missirlian M. *et al* 2023 Overview related to manufacturing, testing and installation of the full tungsten actively cooled ITER-like divertor in the WEST tokamak *29th IAEA Fusion Energy Conf.* (*London, 16–21 October 2023*) [IAEA–CN–316-1989]
[4] Ramaniraka M., Richou M., Vignal N., Addab Y. and Missirlian M. 2022 *Nucl. Mater. Energy* **32** 101210
[5] Chanet N. *et al* 2021 *Fusion Eng. Des.* **166** 112376
[6] Anquetin Y., Gaspar J., Corre Y., Tichit Q., Gardarein J.L., Laffont G., Missirlian M. and Pocheau C. 2023 *Fusion Eng. Des.* **190** 113480
[7] Dejarnac R., Sestak D., Gunn J.P., Firdaouss M., Greuner H., Pascal J.-Y., Richou M. and Roche H. 2021 *Fusion Eng. Des.* **163** 112120
[8] Giruzzi G. *et al* 2009 *Nucl. Fusion* **49** 104010
[9] Gaspar J. *et al* 2021 *Nucl. Fusion* **61** 096027
[10] Klepper C.C. *et al* 2022 *Plasma Phys. Control. Fusion* **64** 104008
[11] Houry M. *et al* 2023 Protection of the divertor and the first wall in the WEST tokamak in view of ITER *29th IAEA Fusion Energy Conf.* (*London, 16–21 October 2023*) [IAEA–CN–316-2137]
[12] Aumeunier M.-H. *et al* 2024 *Nucl. Fusion* **64** 086044
[13] Corre Y. *et al* 2023 *Nucl. Mater. Energy* **37** 101546
[14] Colas L. *et al* 2023 "Tungsten gross erosion and plasma impurity contamination in WEST Phase 1: a statistical comparison of LH and ICRF-heated L-mode plasmas *29th IAEA Fusion Energy Conf.* (*London, 16–21 October 2023*) [IAEA–CN–316-2045]
[15] Goniche M. *et al* 2022 *Nucl. Fusion* **62** 126058
[16] Di Genova S. *et al* 2023 *Nucl. Mater. Energy* **34** 101340
[17] Ciraolo G. *et al* 2023 Modeling impurity sources, transport and screening in edge tokamak plasmas: comparison with WEST experiments and applications to ITER scenarios *29th IAEA Fusion Energy Conf.* (*London, 16–21 October 2023*) [IAEA–CN–316-1954]
[18] Scotto D'abusco M., Giorgiani G., Artaud J.F., Bufferand H., Ciraolo G., Ghendrih P., Serre E. and Tamain P. 2022 *Nucl. Fusion* **62** 086002
[19] Meyer O. *et al* 2016 *Rev. Sci. Instrum.* **87** 11E309
[20] Devynck P., Fedorczak N., Mao R. and Vartanian S. 2021 *J. Phys. Commun.* **5** 095008
[21] Guirlet R., Desgranges C., Schwob J.L., Mandelbaum P. and Boumendjel M.Y. 2022 *Plasma Phys. Control. Fusion* **64** 105024

[22] Ostuni V. *et al* 2022 *Nucl. Fusion* **62** 106034
[23] Peysson Y. *et al* 2023 The HARMONIA project: a joint effort to study the interplay between heavy impurity transport and the current density profile driven by the Lower Hybrid wave in the WEST tokamak *29th IAEA Fusion Energy Conf.* (*London, 16–21 October 2023*) [IAEA-CN-316-2006]
[24] Moiraf D., Morales J., Colas L., Fedorczak N., Gaspar J. and Dumont R. 2023 *Nucl. Fusion* **63** 086010
[25] Maget P. *et al* 2023 *Plasma Phys. Control. Fusion* **65** 125009
[26] Morales J. *et al* 2023 Improving physical understanding and plasma performances in WEST *49th EPS Conf. on Plasma Physics 2023* (*Bordeaux, France*) submitted
[27] Delpech L. *et al* 2023 *Fusion Eng. Des.* **186** 113360
[28] Dumont R. 2009 *Nucl. Fusion* **49** 075033
[29] Dumont R. and Zarzoso D. 2013 *Nucl. Fusion* **53** 013002
[30] Bourdelle C. *et al* 2023 *Nucl. Fusion* **63** 056021
[31] Verdoolaege G. *et al* 2021 *Nucl. Fusion* **61** 076006
[32] Frassinetti L. *et al* 2021 *Nucl. Fusion* **61** 016001
[33] Beurskens M.N.A. *et al* 2022 *Nucl. Fusion* **62** 016015
[34] Artaud J.F. *et al* 2018 *Nucl. Fusion* **58** 105001
[35] Van de Plassche K.L., Citrin J., Bourdelle C., Camenen Y., Casson F.J., Dagnelie V.I., Felici F., Ho A. and Van Mulders S. 2020 *Phys. Plasmas* **27** 022310
[36] Manas P., Artaud J.-F., Bourdelle C., Ostuni V., Morales J. and Citrin J. 2024 *Nucl Fusion* **64** 036011

[37] Maget P. *et al* 2022 *Plasma Phys. Control. Fusion* **64** 045016
[38] Bernert M. *et al* 2021 *Nucl. Fusion* **61** 024001
[39] Glöggler S. *et al* 2019 *Nucl. Fusion* **59** 126031
[40] Bodner G. *et al* 2022 *Nucl. Fusion* **62** 086020
[41] Bodner G. *et al* 2024 *Nucl. Fusion* **64** 045022
[42] Lunsford R. *et al* 2023 Plasma modification and wall conditioning through boron particulate injection in the full tungsten environment of WEST *29th IAEA Fusion Energy Conf.* (*London, 16–21 October 2023*) [IAEA–CN–316-2304]
[43] Silvagni D. *et al* 2024 *Phys. Plasmas* **31** 022501
[44] Joffrin E. *et al* 2017 *Nucl. Fusion* **57** 086025
[45] Gaspar J. *et al* 2024 *Nucl. Fusion* **64** 036018
[46] Corre Y. *et al* 2021 *Fusion Eng. Des.* **170** 112528
[47] Gaspar J. *et al* 2022 *Nucl. Fusion* **62** 096023
[48] Tsitrone E. *et al* 2023 Overview of material migration and fuel retention in the full tungsten tokamak WEST after the first phase of operation *29th IAEA Fusion Energy Conf.* (*London, 16–21 October 2023*) [IAEA–CN–316-1821]
[49] Balden M. *et al* 2021 *Phys. Scr.* **96** 124020
[50] Diez M. *et al* 2023 *Nucl. Mater. Energy* **34** 101399
[51] Richou M. *et al* 2024 *Nucl. Fusion* accepted
[52] Durif A., Richou M., Bergheau J.-M., Gallais L., Kermouche G. and Pintsuk G. 2022 *J. Nucl. Mater.* **569** 153906
[53] Brezinsek S. *et al* 2019 *Nucl. Fusion* **59** 096035